Mondal *EURASIP Journal on Wireless Communications and Networking* (2016) 2016:238
DOI 10.1186/s13638-016-0741-y

EURASIP Journal on Wireless Communications and Networking

RESEARCH Open Access

Impact of spatial sampling frequency offset and motion blur on optical wireless systems using spatial OFDM

M. Rubaiyat H. Mondal

Abstract

Pixelated communication systems can convey high-speed data over optical wireless channels by using *spatial orthogonal frequency division multiplexing* (spatial OFDM) modulation. Two forms of spatial OFDM, spatial asymmetrically clipped optical OFDM (SACO-OFDM) and spatial dc-biased optical OFDM (SDCO-OFDM), have been considered in the literature of pixelated communication. This paper mathematically describes the SACO-OFDM signal and then proposes a power-efficient derivative of SACO-OFDM termed as *noise-cancelled spatial OFDM* (NCS-OFDM). However, NCS-OFDM and other spatial OFDM systems can be impaired by *spatial sampling frequency offset* (SSFO) defined as the difference in the number of transmitted and received pixels and by coexisting defocus and motion blur forming an *asymmetric point spread function* (APSF). In this paper, for the first time, the effects of SSFO and APSF on a spatial OFDM based pixelated system are investigated. Simulation results show that both SSFO and APSF cause phase distortions and attenuation of the data-carrying spatial-subcarriers resulting in bit error rate (BER) degradation. Simulation results also indicate that in the presence of several channel impairments including SSFO and APSF, NCS-OFDM outperforms SACO-OFDM and SDCO-OFDM in terms of power efficiency.

Keywords: Motion blur, Noise, OFDM, Optical wireless communication, Pixels, Pixelated systems, Spatial OFDM

1 Introduction

In recent years, wireless data traffic has experienced enormous growth due to the increase in bandwidth-intensive applications such as video streaming, voice over IP and network-attached storage. Consequently, the radio frequency (RF) spectrum is becoming more and more congested. Multiple-input multiple-output (MIMO) optical wireless communication (OWC) [1–10] is considered as a supplemental technology to RF links for many high data rate applications. MIMO OWC can have either a non-imaging or an imaging receiver. Research has shown that MIMO systems using non-imaging concentrators do not perform well at many receiver positions, and consequently, little diversity gain is obtained. The use of an imaging receiver may overcome this problem [8]. One form of imaging system is pixelated OWC [11–19], where the term pixelated means that the optical modulator, the transmitted images and the detector are each composed of a large number of smaller units. Figure 1 illustrates pixelated communication where a number of image frames are used to carry the data. Such a system operates based on image transfer. For pixelated OWC, a pixelated grid of light-emitting diodes (LEDs) or a liquid crystal display (LCD) screen can be used as a transmitter. In addition, arrays of pixel sources found in devices such as TVs, display walls, lighting and electronic billboards may also be considered as such transmitters. On the other hand, an imaging lens along with an array of photodiodes or a stand-alone camera can be used as a receiver [11, 14]. In between the transmitter and the receiver, a two dimensional (2-D) optical wireless channel is described by its spatial impulse response known as the point spread function (PSF).

Pixelated systems may provide high transmission rates by exploiting spatial diversity at a large scale. A number of recent proof-of-concept experiments reported in [11, 14, 15] have demonstrated the feasibility

Correspondence: rubaiyat97@yahoo.com
Institute of Information and Communication Technology (IICT), Bangladesh University of Engineering and Technology (BUET), Dhaka, Bangladesh

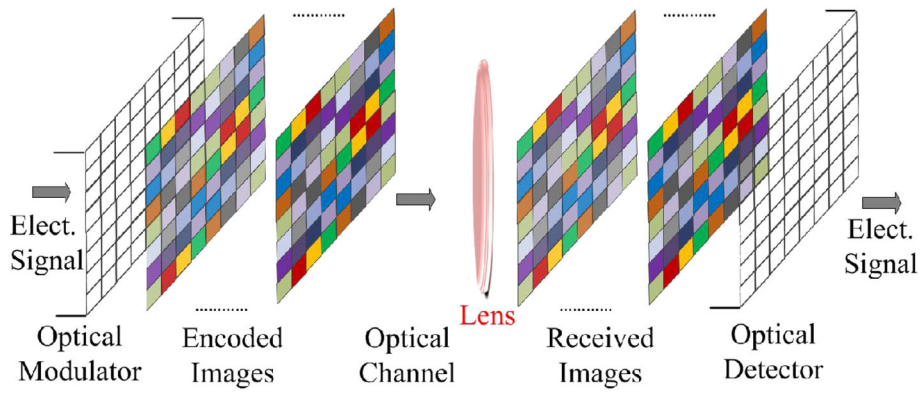

Fig. 1 Illustration of a pixelated OWC system

of pixelated communication. Such a system has the potential to provide a well-directed secure link for inter-device communication of gigabytes of data. Therefore, these links can be used for a number of near-field communication applications such as mobile advertisements, secure data communication, data transfer in dense high-contention scenarios and vehicle-to-traffic light communication [14]. However, the pixelated transmitter has to be within the field of view of the imaging receiver [11], limiting the extent of user mobility, and thus, systems of this type may not be suitable for some application areas.

In order to transmit data in parallel, a pixelated system may apply *spatial orthogonal frequency division multiplexing* (spatial OFDM) [11, 14, 18, 20–22], which is essentially an extension of the conventional OFDM concept [23–25] to the 2-D spatial domain. For spatial OFDM modulation, information is encoded using several orthogonal 2-D subcarriers in the spatial-frequency domain which is the frequency representation of the 2-D image space. Each of the 2-D spatial OFDM frames is transformed into a pixelated image. These images are transmitted into the 2-D optical channel. For pixelated OWC, spatial OFDM exhibits a number of advantages compared to systems that encode data directly in the spatial domain. For instance, the use of spatial OFDM algorithms at the transmitter side allows generating data-carrying images in a way that makes them much robust to 2-D spatial distortions. Consequently, the receiver can apply simple correction algorithms to decode the images [14, 18, 26, 27].

However, the technology of spatial OFDM based pixelated systems is still in its infancy and has to overcome several challenges including power constraints, spatial distortions [18, 27–29] and temporal distortions [16, 30]. Limiting factors such as ambient light [14], spatial perspective distortions [14], spatial rotational error [19] and temporal synchronization problems [16] have been studied in the literature. In recent years, the author of this paper has analysed the effects of spatial distortions such as defocus blur [28, 29], vignetting [18] and fractional misalignment error [27]. The results reported in the above-mentioned previous studies are based on the assumption that the numbers of pixels in the transmitted images and the corresponding received images are the same. In other words, the numbers of received pixels in each dimension are equal to the numbers of transmitted pixels in the corresponding dimension, i.e. the value of spatial sampling frequency offset (SSFO) is zero where each pixel is a spatial sample. However, this is unlikely in many practical pixelated systems. Furthermore, the effects of coexisting defocus and motion blur which can be jointly described by an asymmetric PSF (APSF) are yet to be studied for spatial OFDM based pixelated communication. It is noteworthy that this combined blur is different from the previously studied stand-alone defocus blur [28] which is usually modelled using a symmetric PSF (SPSF).

In this paper, the underlying characteristics of a popular form of spatial OFDM termed as *spatial asymmetrically clipped optical OFDM* (SACO-OFDM) [26] are mathematically studied. Based on the analysis, a noise cancellation technique is applied to form noise-cancelled spatial OFDM (NCS-OFDM). Next, for spatial OFDM, the effects of SSFO and APSF are studied. Computer simulations are performed to evaluate and compare the bit error rate (BER) performance of SACO-OFDM, spatial dc-biased optical OFDM (SDCO-OFDM) and NCS-OFDM in the presence of SSFO, APSF, vignetting, fractional misalignment and additive white Gaussian noise (AWGN).

The remainder of this paper is organized as follows: Section 2 describes a spatial OFDM based pixelated system. Section 3 analyses an SACO-OFDM signal and then proposes an appropriate noise cancellation technique. In Section 4, SSFO and APSF are described for the case of spatial OFDM. Simulation results on the performance of SACO-OFDM, SDCO-OFDM and NCS-OFDM impaired by a number of channel perturbations including SSFO,

APSF and AWGN are presented in Section 5. The paper concludes in Section 6.

2 System design

In pixelated OWC using spatial OFDM, data are embedded in the 2-D spatial-frequency domain, the frequency equivalence of the 2-D spatial domain. In this section, SACO-OFDM will be considered as a spatial-frequency domain encoder. Figure 2a shows the block diagram of an SACO-OFDM-based pixelated communication scheme. Figure 2b illustrates the optical intensity, and Fig. 2c presents the corresponding image for a single SACO-OFDM

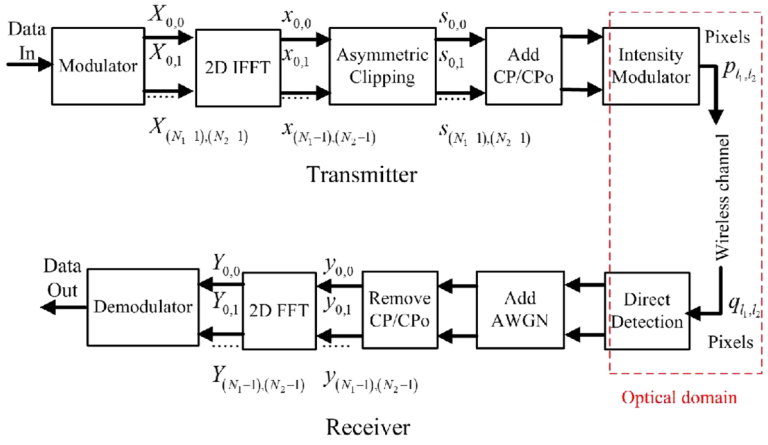

(a)

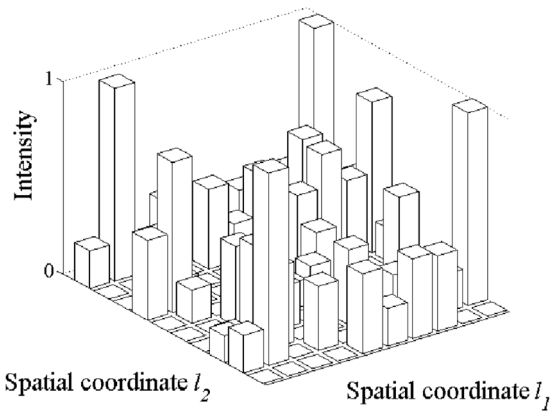

(b)

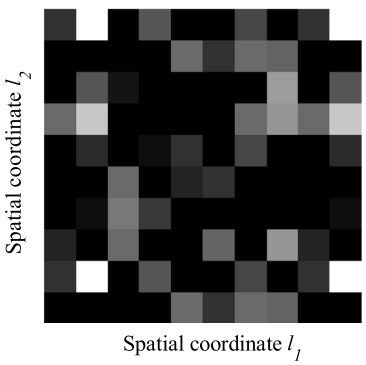

(c)

Fig. 2 **a** Block diagram of an SACO-OFDM-based pixelated system. **b** Transmitted optical intensity in the 2-D spatial domain. **c** Transmitted greyscale image frame

frame. The transmission and the reception methods and the performance metric of the overall system are discussed in the following.

2.1 Transmitter

Consider first the SACO-OFDM transmitter. For each of the transmitted SACO-OFDM frames, the data are mapped to quadrature amplitude modulation (QAM) constellation points resulting in a matrix $\mathbf{X}$ where the even-index columns are set to zero [26]:

$$\mathbf{X} = \begin{pmatrix} 0 & X_{0,1} & 0 & \dots & X_{0,N_2-1} \\ 0 & X_{1,1} & 0 & \cdots & X_{1,N_2-1} \\ & \vdots & & \ddots & \ddots \\ 0 & X_{N_1-1,1} & 0 & & X_{N_1-1,\,N_2-1} \end{pmatrix}. \quad (1)$$

Note that the elements of $\mathbf{X}$ are in the spatial-frequency domain. For the remaining of the paper, the terms *odd subcarriers* and *even subcarriers* will be used to refer to the subcarriers corresponding to the odd-index and even-index columns of $\mathbf{X}$, respectively. So X_{k_1,k_2} represents the signal on the (k_1, k_2)th subcarrier, where k_1 and k_2 are integers between 0 and $N_1 - 1$ and 0 and $N_2 - 1$, respectively. Since the optical signal from the transmitter panel will be in the spatial domain, the term $\mathbf{X}$ has to be transformed to a spatial domain signal of non-complex and non-negative values. Note that a 2-D inverse fast Fourier transform (IFFT) is a means of converting a spatial-frequency domain signal to its corresponding spatial domain version. In order to ensure that the 2-D IFFT output of $\mathbf{X}$ will result in a real-valued matrix $\mathbf{x}$, Hermitian symmetry [26] is maintained for $\mathbf{X}$. The elements of $\mathbf{x}$ are denoted here as x_{l_1,l_2} where (l_1, l_2) is the 2-D spatial index and l_1 and l_2 are integers between 0 and $N_1 - 1$ and 0 and $N_2 - 1$, respectively. Using the formula for 2-D IFFT, the term x_{l_1,l_2} can be expressed as follows:

$$x_{l_1,l_2} = \frac{1}{N_1 N_2} \sum_{k_1=0}^{N_1-1} \sum_{k_2=0}^{N_2-1} X_{k_1,k_2} \exp\left(\frac{j2\pi k_1 l_1}{N_1} + \frac{j2\pi k_2 l_2}{N_2}\right). \quad (2)$$

The signal x_{l_1,l_2} is bipolar, and it is converted to a unipolar signal s_{l_1,l_2} [26] by asymmetrical clipping at the zero-amplitude level. So:

$$s_{l_1,l_2} = \begin{cases} 0, & x_{l_1,l_2} < 0 \\ x_{l_1,l_2}, & x_{l_1,l_2} \geq 0. \end{cases} \quad (3)$$

Next, cyclic extensions in the form of a cyclic prefix (CP) and a cyclic postfix (CPo) [29] are added to both the rows and the columns of $\mathbf{s}$, the corresponding matrix form of s_{l_1,l_2}. The term $\mathbf{s}$ which represents a spatial OFDM frame in the electrical domain is then applied to the input of the intensity modulator.

At the intensity modulator, the smallest unit of a light source is considered as a *transmitter pixel*. The number of pixels on an LCD screen is usually much greater than that of a grid of LED arrays. An intensity modulator may experience nonlinear distortions because of its physical limitations. Therefore, the electrical signal has to be within the dynamic range of the modulator. For instance, the amplitude of the input electrical signal has to be quantized to 256 levels for an 8-bit intensity modulator. The intensity modulator form images by assigning each transmitter pixel an intensity value proportional to the input electrical signal. Note that for the particular case of red-green-blue (RGB) intensity modulation, the electrical signal is mapped to the intensity values of each colour channel. The data-carrying transmitted image is usually formed at the middle of the intensity modulator with the pixels outside the frame turned off. For the rest of this paper, the term *transmitted pixels* will be used to denote the pixels corresponding to only the data-carrying transmitted image. The optical signal from the transmitted pixels forms the time-varying sequence of images. In other words, each of the spatial OFDM frames in the electrical domain is converted to an image frame in the optical domain. Figure 2b shows an example of the optical intensity emitted from an intensity modulator where the peak value of the electrical sample is normalized to have a value of unity. Figure 2c presents the pixelated image frame where the intensities are converted into greyscale values. It can be seen that the pixels having the maximum and the minimum intensity in Fig. 2b are represented in Fig. 2c as complete white and complete dark pixels, respectively. Note that for clarity, Figs. 2b, c are illustrated for a small SACO-OFDM frame of only 10×10 pixels. Mathematically, the intensity of the transmitted pixels, p_{l_1,l_2}, can be written as $p_{l_1,l_2} = \varsigma s_{l_1,l_2}$ where ς is the electrical-to-optical conversion efficiency [18]. Without loss of generality, the term ς can be assumed to be unity. Therefore, the transmitted optical signal from the pixels can be related to the input electrical signal as:

$$p_{l_1,l_2} = s_{l_1,l_2}. \quad (4)$$

Throughout this paper, it is considered that a single transmitted image frame is mapped to only a single spatial OFDM electrical frame. Note that the overall information transmission rate is a function of the frame rate, the number of pixels per frame, the number of colour channels and the number of bits per pixel.

2.2 Receiver

Now consider the SACO-OFDM receiver. In the case of indoor pixelated OWC, the optical channel varies slowly in time and therefore can be assumed to be static. For proper data transfer, the imaging receiver has to have the transmitter panel within its field of view. In addition, the transmitter plane and the receiver plane are to be kept parallel to overcome the perspective distortion. To recover data from each of the transmitted image frame, the receiver capture rate is usually kept twice the transmitter refresh rate. When these conditions are met, the receiver imaging lens attempts to concentrate the light from each transmitter pixel onto a small region in the photodetector. In other words, the lens reproduces the images on an array of receiver pixels. These pixels receive light signals from a number of sources, such as the data-carrying transmitted pixels, the unused transmitter pixels and the illumination outside the transmitter. In order to separate the wanted pixels, signal-processing techniques are applied to the total image. The data-carrying received image is extracted from the total captured image by detecting the four corners. For the rest of this paper, the term received pixels will be used to denote only the pixels corresponding to the data-carrying received images. Mathematically, the intensity of the received pixels, q_{l_1,l_2}, can be expressed as a function of p_{l_1,l_2} and the system PSF, h_{l_1,l_2}:

$$q_{l_1,l_2} = p_{l_1,l_2} \otimes h_{l_1,l_2} \tag{5}$$

where '⊗' is the 2-D convolution operator. Next, q_{l_1,l_2} is converted back to the electrical domain by the direct detection detectors. The obtained electrical signal experiences channel noise, z_{l_1,l_2}, which is often composed of shot noise and thermal noise. This noise can be modelled as AWGN similar to other studies [18]. The CP and CPo are then deducted from the noisy signal. The resultant electrical signal, y_{l_1,l_2}, can be written in the following form using (5) and (4) [18]:

$$\begin{aligned} y_{l_1,l_2} &= q_{l_1,l_2} + z_{l_1,l_2} \\ &= s_{l_1,l_2} \otimes h_{l_1,l_2} + z_{l_1,l_2} \end{aligned} \tag{6}$$

where it is assumed that the responsivity of the photodetecting elements, R_p, is unity. A 2-D FFT is then performed on y_{l_1,l_2}, resulting in Y_{k_1,k_2}, the signal on the received subcarriers:

$$Y_{k_1,k_2} = S_{k_1,k_2} H_{k_1,k_2} + Z_{k_1,k_2} \tag{7}$$

where S_{k_1,k_2}, H_{k_1,k_2} and Z_{k_1,k_2} are the spatial-frequency domain representations of s_{l_1,l_2}, h_{l_1,l_2} and z_{l_1,l_2}, respectively. Moreover, S_{k_1,k_2} is a function of the original subcarriers, X_{k_1,k_2}, as will be shown in (16) in Section 3.1. Finally, the term Y_{k_1,k_2} is corrected using a single-step equalizer, and then the resultant signal is demodulated to perform the estimation of the input data.

2.3 Performance metric

A pixelated system can use different variants of spatial OFDM modulation. Comparing spatial OFDM modulation schemes is not straightforward as the BER depends on the signal-to-noise ratio (SNR) of the electrical signal obtained from the direct detection receiver, whereas the transmitted average optical power is considered as the limiting factor [26]. When the transmitted electrical signal is s_{l_1,l_2}, the average optical power, i.e. the optical power per pixel, depends on $E\{s_{l_1,l_2}\}$ where $E\{\bullet\}$ is the expectation operator. On the other hand, the average electrical power, i.e. the electrical power per pixel, depends on $E\left\{s_{l_1,l_2}^2\right\}$. Hence, the conversion between optical power and electrical power depends on the statistics of s_{l_1,l_2}. Since for different spatial OFDM schemes the term s_{l_1,l_2} will have different statistics, the conversion from optical to electrical power will be different. Similar to the work in [26], the average optical power here is defined as $E\{s_{l_1,l_2}\}$ and the average electrical power as $E\left\{s_{l_1,l_2}^2\right\}$. For a fixed value of $E\{s_{l_1,l_2}\}$, the spatial OFDM form with high electrical power to optical power ratio $E\left\{s_{l_1,l_2}^2\right\}/E\{s_{l_1,l_2}\}$ is likely to ensure better BER performance. With this consideration, two performance metrics are used in this paper to compare different spatial OFDM modulation. These metrics are $E_{b(\mathrm{elec})}/N_0$ and $E_{b(\mathrm{opt})}/N_0$ where $E_{b(\mathrm{elec})}$ is the received electrical energy per bit, $E_{b(\mathrm{opt})}$ is the received optical energy per bit and N_0 is the single-sided noise spectral density. The terms $E_{b(\mathrm{elec})}$ and $E_{b(\mathrm{opt})}$ can be mathematically described as $E_{b(\mathrm{elec})} = E\left\{s_{l_1,l_2}^2\right\}/L$ and $E_{b(\mathrm{opt})} = E\{s_{l_1,l_2}\}/L$, respectively, where L represents the number of bits per pixel. Moreover, the term N_0 can be expressed as $N_0 = E\left\{\left|z_{l_1,l_2}\right|^2\right\}$. Unlike the electrical domain term $E_{b(\mathrm{elec})}/N_0$, $E_{b(\mathrm{opt})}/N_0$ takes into account the optical-to-electrical conversion efficiency of the system, and thus the BER versus $E_{b(\mathrm{elec})}/N_0$ graph will be different from the BER against $E_{b(\mathrm{opt})}/N_0$ graph.

3 Study of SACO-OFDM and NCS-OFDM signals

3.1 Analysis of SACO-OFDM signal

In this section, it will be shown that the SACO-OFDM signal exhibits anti-symmetry property in the spatial domain and that the signal is effectively unaffected by clipping noise in the spatial-frequency domain. Firstly, the SACO-OFDM signal will be analysed in the spatial domain by adapting the analysis of temporal OFDM shown in [31].

It is shown in Section 2 that only the odd subcarriers (where k_2 is odd) of SACO-OFDM are used for data transmission, so (2) can be modified to give:

$$x_{l_1,(l_2+N_2/2)} = \frac{1}{N_1N_2}\sum_{k_1=0}^{N_1-1}\sum_{k_2=0}^{N_2-1} X_{k_1,k_2}\ \exp\left\{\frac{j2\pi k_1 l_1}{N_1}+\frac{j2\pi k_2(l_2+N_2/2)}{N_2}\right\} \quad (8)$$
$$= \frac{1}{N_1N_2}\sum_{k_1=0}^{N_1-1}\sum_{k_2=0}^{N_2-1} X_{k_1,k_2}\ \exp\left\{\frac{j2\pi k_1 l_1}{N_1}+\frac{j2\pi k_2 l_2}{N_2}\right\}\exp(j\pi k_2).$$

For the data-carrying SACO-OFDM signal, k_2 is odd and so

$$\exp(j\pi k_2) = -1. \quad (9)$$

Using (2) and (9), (8) can be modified as:

$$x_{l_1,(l_2+N_2/2)} = -\frac{1}{N_1N_2}.\sum_{k_1=0}^{N_1-1}\sum_{k_2=0}^{N_2-1} X_{k_1,k_2}\ \exp\left\{\frac{j2\pi k_1 l_1}{N_1}+\frac{j2\pi k_2 l_2}{N_2}\right\}$$
$$= -x_{l_1,l_2} \quad (10)$$

This is the *anti-symmetry property* across one dimension (1-D). This anti-symmetry feature of the SACO-OFDM spatial samples will be used in Section 3.2 to identify which samples of the received signal are most likely to be due to channel noise. This is important in formulating the noise cancellation technique for SACO-OFDM.

Next, the SACO-OFDM signal will be analysed in the spatial-frequency domain. This will be carried out by expressing the received signal Y_{k_1,k_2} mentioned in (7) in terms of the input signal X_{k_1,k_2}. The term X_{k_1,k_2} which is the spatial-frequency domain equivalence of x_{l_1,l_2} can be written in the following form:

$$X_{k1,k2} = \sum_{l_1=0}^{N_1-1}\sum_{l_2=0}^{N_2-1} x_{l_1,l_2}\exp\left(\frac{-j2\pi k_1 l_1}{N_1}+\frac{-j2\pi k_2 l_2}{N_2}\right) \quad (11)$$

Separating out the positive and negative values of x_{l_1,l_2} gives:

$$X_{k_1,k_2} = \sum_{l_1=0}^{N_1-1}\sum_{\substack{l_2=0\\ x_{l_1,l_2}>0}}^{N_2/2-1}\left[x_{l_1,l_2}\ \exp\left(\frac{-j2\pi k_1 l_1}{N_1}+\frac{-j2\pi k_2 l_2}{N_2}\right) + x_{l_1,(l_2+N_2/2)}\ \exp\left\{\frac{-j2\pi k_1 l_1}{N_1}+\frac{-j2\pi k_2(l_2+N_2/2)}{N_2}\right\}\right] +$$
$$+\sum_{l_1=0}^{N_1-1}\sum_{\substack{l_2=0\\ x_{l_1,l_2}<0}}^{N_2/2-1}\left[x_{l_1,l_2}\ \exp\left(\frac{-j2\pi k_1 l_1}{N_1}+\frac{-j2\pi k_2 l_2}{N_2}\right) + x_{l_1,(l_2+N_2/2)}\ \exp\left\{\frac{-j2\pi k_1 l_1}{N_1}+\frac{-j2\pi k_2(l_2+N_2/2)}{N_2}\right\}\right]. \quad (12)$$

Equation (12) can be simplified to give:

$$X_{k_1,k_2} = \sum_{l_1=0}^{N_1-1}\sum_{\substack{l_2=0\\ x_{l_1,l_2}>0}}^{N_2/2-1}\left\{x_{l_1,l_2}+x_{l_1,(l_2+N_2/2)}\ \exp(-j\pi k_2)\right\} \times \exp\left(\frac{-j2\pi k_1 l_1}{N_1}+\frac{-j2\pi k_2 l_2}{N_2}\right)$$
$$+\sum_{l_1=0}^{N_1-1}\sum_{\substack{l_2=0\\ x_{l_1,l_2}<0}}^{N_2/2-1}\left\{x_{l_1,l_2}+x_{l_1,(l_2+N_2/2)}\ \exp(-j\pi k_2)\right\} \times \exp\left(\frac{-j2\pi k_1 l_1}{N_1}+\frac{-j2\pi k_2 l_2}{N_2}\right). \quad (13)$$

Using (9) and (10), (13) can be rewritten as follows:

$$X_{k_1,k_2} = \sum_{l_1=0}^{N_1-1}\sum_{\substack{l_2=0\\ x_{l_1,l_2}>0}}^{N_2/2-1} 2x_{l_1,l_2}\ \exp\left(\frac{-j2\pi k_1 l_1}{N_1}+\frac{-j2\pi k_2 l_2}{N_2}\right)$$
$$+\sum_{l_1=0}^{N_1-1}\sum_{\substack{l_2=0\\ x_{l_1,l_2}<0}}^{N_2/2-1} 2x_{l_1,l_2}\ \exp\left(\frac{-j2\pi k_1 l_1}{N_1}+\frac{-j2\pi k_2 l_2}{N_2}\right). \quad (14)$$

Note that $X_{k1,k2}$ is the 2-D FFT of the bipolar signal x_{l_1,l_2} which is clipped to form unipolar signal s_{l_1,l_2} as shown in (3). So S_{k_1,k_2}, which is the 2-D FFT of s_{l_1,l_2}, can be obtained from (14) as follows:

$$S_{k_1,k_2} = \sum_{l_1=0}^{N_1-1}\sum_{\substack{l_2=0\\ x_{l_1,l_2}>0}}^{N_2/2-1} 2x_{l_1,l_2}\ \exp\left(\frac{-j2\pi k_1 l_1}{N_1}+\frac{-j2\pi k_2 l_2}{N_2}\right). \quad (15)$$

The comparison of (14) and (15) results in:

$$S_{k_1,k_2} = \frac{X_{k_1,k_2}}{2},\ \ k_2 \text{ odd}. \quad (16)$$

Therefore, the odd subcarriers are halved and free from the clipping noise produced from the clipping of x_{l_1,l_2} at the zero-amplitude level. This noise due to clipping falls on the remaining even subcarriers. Using (16), (7) can now be modified to form the SACO-OFDM received signal:

$$Y_{k_1,k_2} = \frac{X_{k_1,k_2}}{2}H_{k_1,k_2} + Z_{k_1,k_2},\ \ k_2 \text{ odd}. \quad (17)$$

So, the only noise source in the received SACO-OFDM signal is the channel noise Z_{k_1,k_2} which will be partially cancelled in Section 3.2 to generate NCS-OFDM.

3.2 Formation of NCS-OFDM signal from SACO-OFDM signal

In this section, the concepts of noise cancellation for temporal OFDM-based OWC systems reported in [32, 33] are combined and then adapted to form a two-stage noise cancellation method for spatial OFDM. First, the transmitter and then the receiver for an NCS-OFDM system are discussed below.

The processing at the NCS-OFDM transmitter is identical to that of a generalized spatial OFDM transmitter described in Section 2. For the bipolar (unclipped) signal x_{l_1,l_2}, the samples at (l_1, l_2) and $(l_1, l_2 + N_2/2)$ are a pair as shown in (10). These two samples have the same value but have opposite polarity. When x_{l_1,l_2} is clipped at zero to form s_{l_1,l_2}, one of the samples of each pair remains positive and the other becomes zero. As for example, consider $\tilde{x}_{l_1,l_2}$ and $\tilde{x}_{l_1,l_2+N_2/2}$ as one of the pair elements where $\tilde{x}_{l_1,l_2+N_2/2}$ is negative-valued, so $\tilde{x}_{l_1,l_2} = -\tilde{x}_{l_1,l_2+N_2/2}$, and after clipping, $\tilde{s}_{l_1,l_2} = \tilde{x}_{l_1,l_2}$ and $\tilde{s}_{l_1,l_2+N_2/2} = 0$. After the addition of CP/CPo, s_{l_1,l_2} is converted to the optical domain.

The NCS-OFDM receiver does some extra processing compared to the stand-alone spatial OFDM receiver mentioned in Section 2. When the transmitted unipolar optical signal is detected at the receiver, the converted electrical signal y_{l_1,l_2} becomes bipolar because of the addition of bipolar channel noise. This noise can then be reduced approximately to half by sequentially applying two noise cancellation techniques. In the first stage of noise cancellation, the samples of y_{l_1,l_2} at (l_1, l_2) and $(l_1, l_2 + N_2/2)$ are inspected. Therefore, the following terms can be obtained:

$$\begin{aligned}\tilde{y}_{l_1,l_2} &= \tilde{s}_{l_1,l_2} \pm \tilde{z}_{l_1,l_2} \\ &= \tilde{x}_{l_1,l_2} \pm \tilde{z}_{l_1,l_2}\end{aligned} \tag{18}$$

and

$$\begin{aligned}\tilde{y}_{l_1,l_2+N_2/2} &= \tilde{s}_{l_1,l_2+N_2/2} \pm \tilde{z}_{l_1,l_2+N_2/2} \\ &= \pm\tilde{z}_{l_1,l_2+N_2/2}.\end{aligned} \tag{19}$$

In this particular example as shown in (18) and (19), $\tilde{y}_{l_1,l_2+N_2/2}$ is the 'noise-only' element. Now, forcing $\tilde{y}_{l_1,l_2+N_2/2}$ to zero amplitude will actually cancel the channel noise at $(l_1, l_2 + N_2/2)$. However, the channel noise component remains in $\tilde{y}_{l_1,l_2}$. For high-SNR scenarios, the term $\tilde{y}_{l_1,l_2+N_2/2}$ is expected to be smaller than $\tilde{y}_{l_1,l_2}$. So, in general, out of the two elements of a y_{l_1,l_2} pair, the element having the smaller amplitude is likely to be the noise-only element and therefore should be set to zero. It can be noted that for the special case where both $\tilde{y}_{l_1,l_2}$ and $\tilde{y}_{l_1,l_2+N_2/2}$ have negative polarity, the one with the higher amplitude value remains unchanged.

In the second stage of noise cancellation, all the remaining negative components of the y_{l_1,l_2} pair are clipped to zero. This ensures that in most cases, approximately half of the channel noise samples of y_{l_1,l_2} are removed which may improve the system performance up to a margin of 3 dB.

4 Effects of SSFO and APSF on spatial OFDM

4.1 SSFO

In a pixelated system, the imaging receiver samples the incoming images in the spatial domain. In practice, it is not possible to adjust the SSFO which has already been defined in Section 1 as the difference in the numbers of pixels in the transmitted and received images. This is because the adjustment of SSFO depends on the pixel size of the receiver and on the distance between the transmitter and the receiver. So, in a practical system, the number of received pixels in each dimension is likely to be different from the number of transmitted pixel in each dimension. This means that if the numbers of transmitted and received pixels (without the CP/CPo) are $N_{T_1} \times N_{T_2}$ and $N_{R_1} \times N_{R_2}$, respectively, then $N_{R_1} \neq N_{T_1}$ and $N_{R_2} \neq N_{T_2}$, respectively. In the following, the SSFO is described with an example.

At the transmitter side, pixels are used to intensity-modulate the $N_1 \times N_2$ electrical samples of $\mathbf{s}$ (without the CP/CPo), where $N_{T_1} = n_1 N_1$ and $N_{T_2} = n_2 N_2$ with n_1 and n_2 being integers. The intensity of the transmitted $N_{T_1} \times N_{T_2}$ pixels is received by the $N_{R_1} \times N_{R_2}$ pixels at the receiving photodetector. The received noisy electrical signal corresponding to $N_{R_1} \times N_{R_2}$ pixels is resampled to $N_1 \times N_2$ electrical samples, where $N_1 = N_{R_1}/m_1$ and $N_2 = N_{R_2}/m_2$. Therefore, $N_{R_1} = m_1' N_{T_1}$ and $N_{R_2} = m_2' N_{T_2}$ where $m_1' = \frac{m_1}{n_1}$ and $m_2' = \frac{m_2}{n_2}$. For the case where $m_1' < 1$ and $m_2' < 1$, the received signal will be distorted due to spatial-averaging effect even for a system with no other impairment. However, for a practical system, the number of the received pixels is likely to be greater than that of the transmitted pixels, i.e. $m_1' > 1$ and $m_2' > 1$. This means each of the transmitted pixels is spread into $m_1' \times m_2'$ received pixels. Consider first the case when m_1' and m_2' are integers; for instance, $m_1' = m_2' = 2$ as shown in Fig. 3a. The intensity of each transmitted pixel will be collected by an integer number (in this case, 4) of received pixels; in other words, no received pixel will get contribution from more than a single transmitted pixel. Consequently, there will be no SSFO induced distortion, i.e. all the received pixels are *unaffected* by SSFO. Now, consider the case where m_1' and m_2' are fractional numbers. This is shown for $m_1' = m_2' = 1.5$

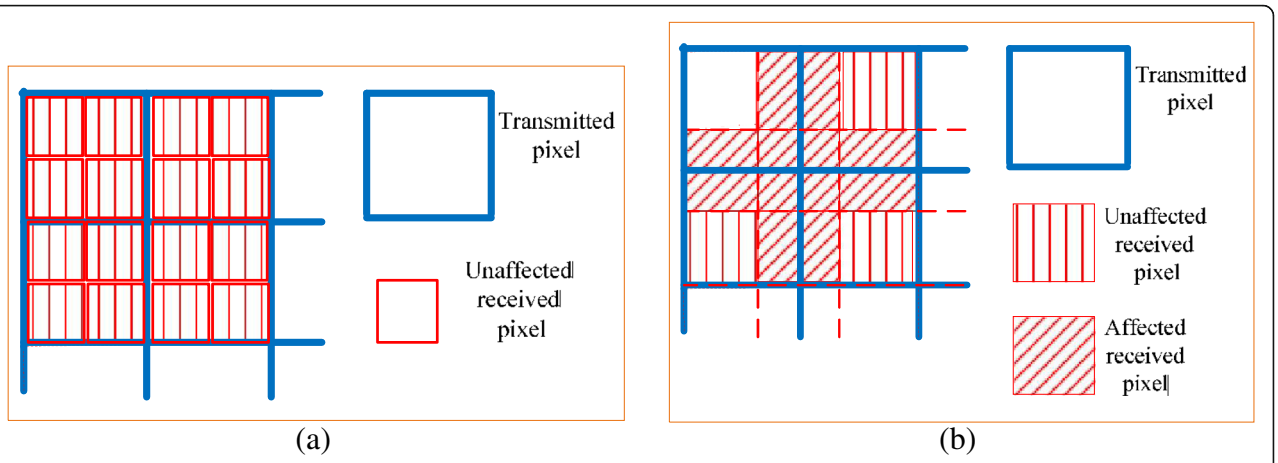

Fig. 3 Illustration of SSFO for **a** $m_1' = m_2' = 2$ and for **b** $m_1' = m_2' = 1.5$

in Fig. 3b. It can be seen that some of the pixels receive contributions from a single transmitted pixel. These pixels are free from SSFO and denoted in the figure as *unaffected* pixels. On the other hand, some pixels receive contributions from more than one transmitted pixel. These pixels are *affected* by SSFO. This will lead to a spatial-averaging effect in the received optical intensity. The higher the values of m_1' and m_2', the lower the ratio of the number of affected pixels to the number of total pixels. Therefore, the spatial-averaging effect reduces for larger values of m_1' and m_2'.

4.2 APSF

The PSF can be termed as the spatial distribution of optical intensity at the receiving detector for a transmitted spatial optical impulse [21, 34]. For the case of an ideal imaging system, the PSF has a distribution of a 2-D Dirac delta function. For the case of a practical imaging system with appropriate focusing, the PSF usually has the distribution of a narrow spatial pulse whose dimensions are mainly a function of the aberrations of the imaging lens and the diffraction phenomenon at the receiver aperture [11]. In a practical pixelated system, both defocus and motion blur are likely to be present. Defocus is the lack of focus of the imaging lens, while motion blur is caused by the relative motion between the transmitter and the receiver during the exposure time of the imaging system. These two blurs together cause the received intensity pattern to be distributed over a larger space, resulting in a degraded PSF. Figure 4 shows the case of defocus-degraded PSF whose elements can be represented as follows (for simplicity, a 3×3 case is shown):

$$h_{l_1,l_2} = \begin{pmatrix} h_{1,-1} & h_{1,0} & h_{1,1} \\ h_{0,-1} & h_{0,0} & h_{0,1} \\ h_{-1,-1} & h_{-1,0} & h_{-1,1} \end{pmatrix}. \tag{20}$$

For the case of a stand-alone defocus blur which is often characterized by a 2-D Gaussian (omnidirectional) SPSF with a spread of σ [28, 35], the elements of (20) are defined as:

$$h_{1,-1} = h_{-1,-1} = h_{1,1} = h_{-1,1} \tag{21}$$

and

$$h_{1,0} = h_{-1,0} = h_{0,1} = h_{0,-1}. \tag{22}$$

On the other hand, it is also difficult to establish a universal model for motion blur since it varies depending on the actual motion during the exposure time of the

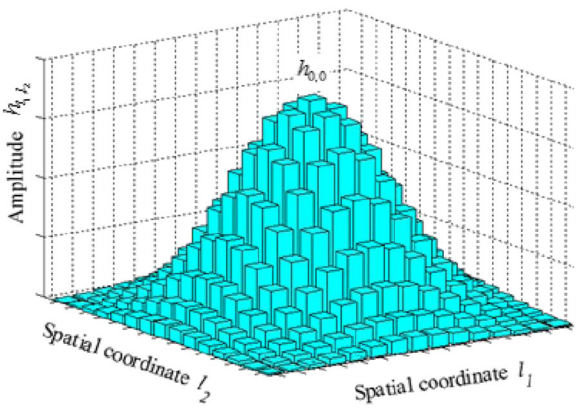

Fig. 4 Illustration of a typical defocus-degraded PSF in the 2-D spatial domain

imaging lens [36]. However, in the literature of photography and image processing [37–40], motion blur is often modelled as simple motion models, e.g. linear constant speed motion. Similarly, in this paper, the motion blur is described as a linear motion across a number of pixels in a single (horizontal or vertical) direction and therefore has an APSF distribution. This is illustrated in Fig. 5. It can be seen that the term h_{l_1,l_2} for APSF has values only in one dimension and obviously does not follow the relationship shown in (21) and (22).

For the case of combined defocus and motion blur, the composite PSF is also asymmetric since it is the convolution of the defocus-degraded PSF and the motion-degraded PSF.

5 Simulation results

In this section, the system performance for SACO-OFDM and NCS-OFDM are evaluated via computer simulations using MATLAB software. In a practical scenario, the numbers of total subcarriers, transmitter/receiver pixels and the magnitudes of channel impairments can vary to a large extent; therefore, there is no standard single value for the simulation parameters. For this paper, the parameters used in the simulations were 256×256 subcarriers having a CP and a CPo of 10 % (rounded up to the next integer) each. Moreover, the level of defocus was set as a spread of 9×9 SPSF with $\sigma = 0.5$. The motion blur was modelled as a linear motion across N_d pixels in the horizontal direction, where $N_d = 1$, 2 and 4. The combination of the defocus blur and the motion blur was used to simulate the effect of APSF. Next, the effect of SSFO was simulated for $m' = 1.5$, 2.5 and 3.5, where $m' = m_1' = m_2'$. For the case of equalization, a single-step spatial-frequency domain equalizer was used. When the higher subcarriers were not used for data transmission, the number of unused higher spatial-frequency index subcarriers in each dimension, N_h, was set equal to $N/2$ where $N_1 = N_2 = N$. In the simulations, the effects of temporal distortions were ignored.

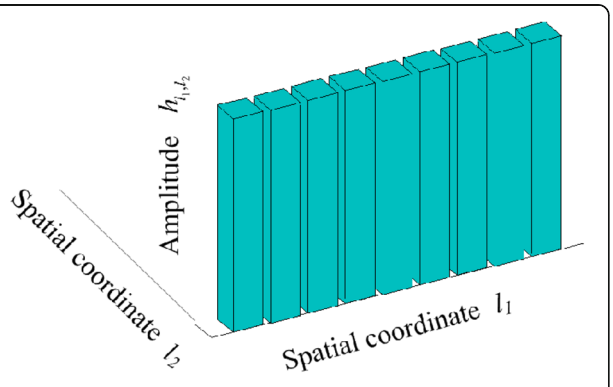

Fig. 5 Illustration of a typical motion-degraded PSF in the 2-D spatial domain

Figure 6 shows the constellation diagrams of the transmitted and the received SACO-OFDM signals. For Figs. 6a, b, the effect of AWGN is ignored to focus on other impairments. Moreover, for clarity only 64×64 subcarriers are used. Figure 6a illustrates the received constellation points for the case of APSF with $N_d = 2$ and $\sigma = 0.5$ as well as for the case of SPSF with $\sigma = 0.5$. It can be seen that the effect of SPSF is only to cause attenuation in the spatial-frequency domain, and the attenuation varies depending on the spatial-frequency index. On the other hand, the effect of APSF is to create both attenuation and phase distortions in the spatial-frequency domain. It is clear that the constellation points experience more spread due to APSF than SPSF. Figure 6b presents the received signal for the case of SSFO where $m' = 1.5$. It can be seen that because of the presence of SSFO, the received constellation points experience attenuation as well as phase distortions.

Figure 7 presents the BER as a function of $E_{b(\mathrm{elec})}/N_0$, the received electrical energy per bit to single-sided noise spectral density, for the case of stand-alone AWGN and SSFO with and without equalization. In this case, the $E_{b(\mathrm{elec})}/N_0$ penalty caused by a particular impairment is calculated, at a BER of 10^{-4}, as the $E_{b(\mathrm{elec})}/N_0$ difference between the plot for that impairment (added with AWGN) and the plot for a stand-alone AWGN system indicated by $m' = 1$. Note that as mentioned in Section 4.1, there is no extra degradation due to SSFO when m' has any integer value of 2. It can be seen that the $E_{b(\mathrm{elec})}/N_0$ penalty due to SSFO is approximately 4.5, 2.8 and 2 dB for $m' = 1.5$, $m' = 2.5$ and $m' = 3.5$, respectively, when there is no equalization. This is because as shown in Section 4.1 the larger the values of m_1' and m_2', the less is the spatial-averaging effect, so the less the power penalty. Hence, the receiver should have more number of pixels than the transmitter to combat the effect of SSFO. It can also be seen from Fig. 7 that the degradation due to SSFO can be further reduced when an equalizer is used and the higher subcarriers are not used to carry the data. However, the unused subcarriers reduce the effective data transmission rate.

Figure 8 presents the BER as a function of $E_{b(\mathrm{elec})}/N_0$, for the case of stand-alone AWGN, SPSF and APSF. All these plots are for the case of equalization with only lower subcarriers carrying data, i.e. $N_h = N/2$. It can be seen that the $E_{b(\mathrm{elec})}/N_0$ penalties due to SPSF with $N_d = 0$, APSF with $N_d = 1$, $N_d = 2$ and $N_d = 4$ are approximately 2, 2.7, 7 and 10 dB respectively. So, the BER degradation is greater for the case of APSF than for SPSF and for greater values of N_d. This is because as shown earlier, the APSF additionally causes phase distortions which is absent in the case of

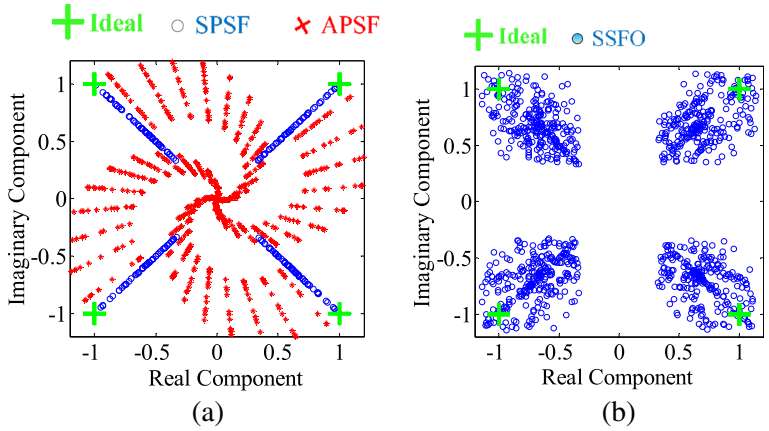

Fig. 6 Constellation diagram for SACO-OFDM for the case of **a** SPSF and APSF and **b** SSFO

SPSF and the level of asymmetry in APSF distribution increases with the increase of N_d. So when motion blur takes place across a greater number of pixels, the BER degradation becomes more prominent.

Figure 9 presents the BER as a function of $E_{b(\text{elec})}/N_0$, for SACO-OFDM and NCS-OFDM. It can be seen that for AWGN-only channels and for a given constellation size of 4-QAM, NCS-OFDM is 2.0 dB better than SACO-OFDM, but the difference increases to 2.7 dB for 16-QAM. This is because for a given power level, larger constellation points are more susceptible to noise and thus cancelling the noise results in more BER improvement. Note that the improvement of 2.7 dB due to noise cancellation is close to the 3-dB improvement as mentioned for an ideal case in Section 3.2. It can also be seen that for the joint case of SSFO with $m' = 1.5$, APSF with $N_d = 2$ and $\sigma = 0.5$ as well as AWGN, 4-QAM NCS-OFDM is only 1 dB better than 4-QAM SACO-OFDM. So the performance difference between NCS-OFDM and SACO-OFDM is reduced in SSFO-APSF channels than stand-alone AWGN channels. Thus, the effectiveness of noise cancellation in NCS-OFDM is dropped when the impairments of SSFO and APSF exist. By comparing the curves for 4-QAM NCS-OFDM in AWGN and SSFO-APSF channels, it can be seen that there can be as large as 8.5 dB degradation in NCS-OFDM due to a given value of SSFO and APSF.

In the following, the BER performance of NCS-OFDM will be compared with that of SACO-OFDM and SDCO-OFDM in terms of average optical power. Since SACO-OFDM/NCS-OFDM uses half the subcarriers of

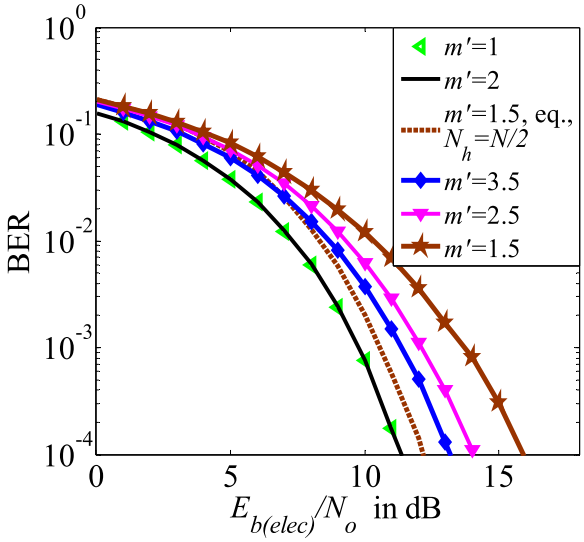

Fig. 7 BER versus $E_{b(\text{elec})}/N_0$ for the case of SSFO. Here, *eq.* stands for equalization and N_h indicates the unused higher subcarriers

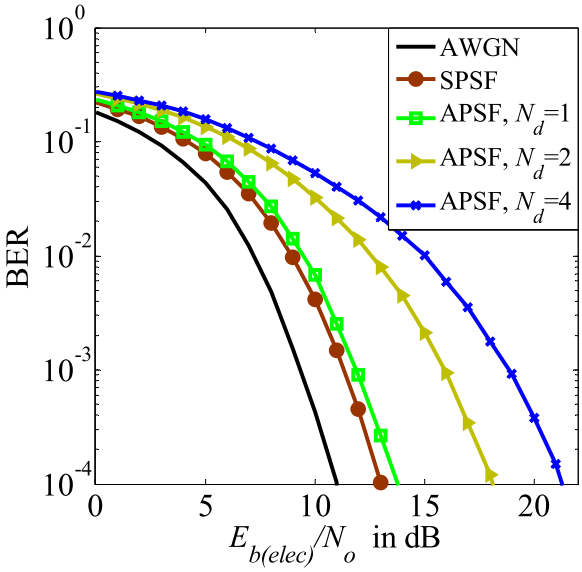

Fig. 8 BER versus $E_{b(\text{elec})}/N_0$ for stand-alone AWGN, SPSF and APSF

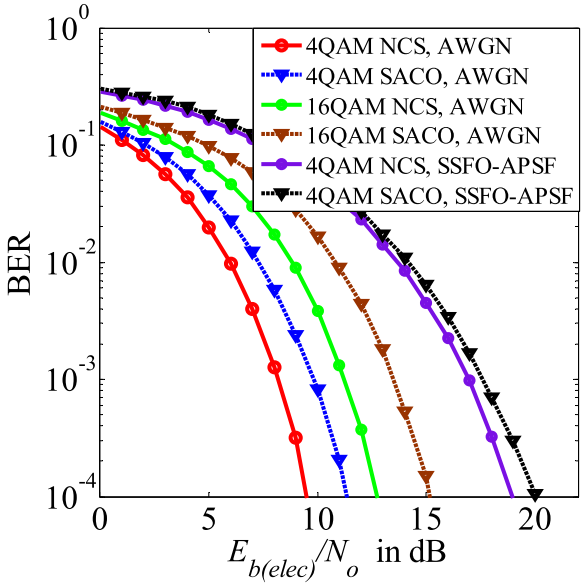

Fig. 9 BER versus $E_{b(\mathrm{elec})}/N_0$ for NCS-OFDM and SACO-OFDM for 4-QAM and 16-QAM constellation points for AWGN and SSFO-APSF channels

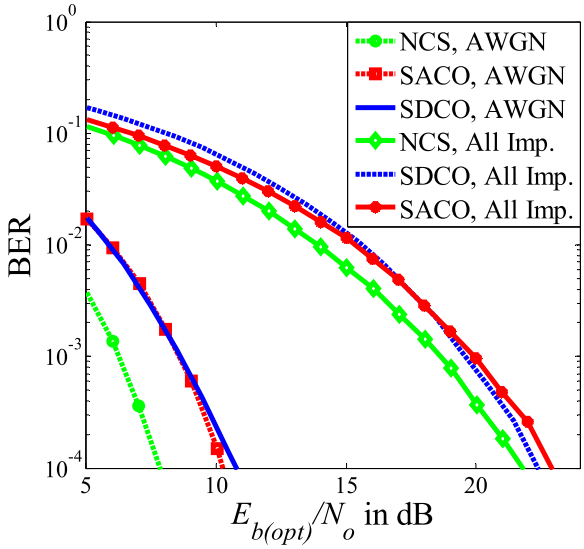

Fig. 10 BER versus $E_{b(\mathrm{opt})}/N_0$ for 16-QAM SACO-OFDM, 4-QAM SDCO-OFDM and 16-QAM NCS-OFDM. *All Imp* indicates the combined impairments of vignetting, misalignment, SSFO, APSF and AWGN

SDCO-OFDM [26], SACO-OFDM/NCS-OFDM with 16-QAM and 256-QAM should be compared with SDCO-OFDM with 4-QAM and 16-QAM, respectively. In a recent study [29], it has been shown that for an optimal bias of $0.80\sigma_x$, SDCO-OFDM with 4-QAM shows better optical power efficiency than SACO-OFDM with 16-QAM for $N_h = N/2$ and for equalization, where σ_x is the standard deviation of x_{l_1,l_2}. The result reported in [29] is for a given value of vignetting and fractional misalignment and SPSF/defocus with a spread of $\sigma = 0.5$. Figure 10 presents the BER as a function of $E_{b(\mathrm{opt})}/N_0$, the received optical energy per bit to single-sided noise spectral density, for NCS-OFDM, SACO-OFDM and SDCO-OFDM with an optimal bias of $0.80\sigma_x$. In this case, the values of vignetting and fractional misalignment are the same as those reported in [29]; SSFO is for $m' = 1.5$, while APSF is for $\sigma = 0.5$ and $N_d = 2$. Figure 10 shows that for a given data rate, for $N_h = N/2$ and for equalization, 16-QAM NCS-OFDM shows better performance than 16-QAM SACO-OFDM and 4-QAM SDCO-OFDM. By comparing the curves for NCS-OFDM in the presence of stand-alone AWGN and all impairments, it is clear that the $E_{b(\mathrm{opt})}/N_0$ penalty due to a given value of vignetting, fractional misalignment error, SSFO and APSF is approximately 14 dB.

6 Conclusions

This paper shows that SSFO and motion blur can impair the BER performance of spatial OFDM based communication systems. The individual presence of SSFO and the simultaneous presence of defocus and motion blur modelled together as APSF cause attenuation and phase distortion in the spatial-frequency domain. However, the effect of SSFO can be decreased by ensuring that the number of received pixels is much larger than the transmitted pixels. Moreover, the use of an equalizer and the use of only the lower subcarriers can further minimize the effect of SSFO. The effect of APSF is different from that of SPSF since SPSF does not cause phase distortion. Depending on the magnitude of motion blur, APSF can create significant BER degradations even when the higher subcarriers are unused for data transmission. Therefore, the relative motion between the transmitter and the receiver must be kept to minimum to ensure reliable data transmission. Next, it is shown that the performance of SACO-OFDM in the joint presence of SSFO and APSF can be improved by forming NCS-OFDM by exploiting the anti-symmetry property of SACO-OFDM. Simulation results show that for a given data rate and for the combined perturbations of vignetting, fractional misalignment, SSFO and APSF, NCS-OFDM shows slightly better optical power efficiency than SACO-OFDM and SDCO-OFDM. Since the above-mentioned impairments can cause $E_{b(\mathrm{opt})}/N_0$ penalty as large as 14 dB, efficient techniques will be required to realize practical compensation of these distortions in a physical system for specific target performance levels.

Competing interests
The author declares that he has no competing interests.

Received: 28 September 2015 Accepted: 24 September 2016
Published online: 04 October 2016

References

1. D Borah, A Boucouvalas, C Davis, S Hranilovic, K Yiannopoulos, A review of communication-oriented optical wireless systems. EURASIP J. Wirel. Commun. Netw. **2012**(1), 91 (2012)
2. K Langer, J Grubor, Recent developments in optical wireless communications using infrared and visible light, in *International Conference on Transparent Optical Networks (ICTON), Rome, Italy*, 2007
3. D O'Brien, M Katz, P Wang, K Kalliojarvi, S Arnon, M Matsumoto et al., Short-range optical wireless communications, in *Technologies for the Wireless Future: Wireless World Research Forum (WWRF)*, 2006, p. 2
4. S Rodriguez Perez, B Rodriguez Mendoza, R Perez Jimenez, O Gonzalez Hernandez, A Garcia-Viera Fernandez, Design considerations of conventional angle diversity receivers for indoor optical wireless communications. EURASIP J. Wirel. Commun. Netw. **2013**(1), 221 (2013)
5. RJ Green, H Joshi, MD Higgins, MS Leeson, Recent developments in indoor optical wireless systems. IET Commun. **2**(1), 3–10 (2008)
6. J-B Wang, X-X Xie, Y Jiao, M Chen, Training sequence based frequency-domain channel estimation for indoor diffuse wireless optical communications. EURASIP J. Wirel. Commun. Netw. **2012**(1), 326 (2012)
7. D O'Brien, R Turnbull, HL Minh, G Faulkner, O Bouchet, P Porcon et al., High-speed optical wireless demonstrators: conclusions and future directions. J. Lightw. Technol. **30**(13), 2181–2187 (2012)
8. L Zeng, D O'Brien, H Minh, G Faulkner, K Lee, D Jung et al., High data rate multiple input multiple output (MIMO) optical wireless communications using white LED lighting. IEEE J. Sel. Areas Commun. **27**(9), 1654–1662 (2009)
9. S Arnon, Optimised optical wireless car-to-traffic-light communication. Transactions on Emerging Telecommunications Technologies **25**(6), 660–665 (2014)
10. B Ghimire, H Haas, Self-organising interference coordination in optical wireless networks. EURASIP J. Wirel. Commun. Netw. **2012**(1), 131 (2012)
11. S Hranilovic, FR Kschischang, A pixelated MIMO wireless optical communication system. IEEE J. Sel. Topics Quantum Electron. **12**(4), 859–874 (2006)
12. HBC Wook, T Komine, S Haruyama, M Nakagawa, Visible light communication with LED-based traffic lights using 2-dimensional image sensor, in *IEEE Consumer Communications and Networking Conference (CCNC)*, 2006
13. A Ashok, M Gruteser, NB Mandayam, J Silva, M Varga, KJ Dana, Challenge: mobile optical networks through visual MIMO, in *International Conference on Mobile Computing and Networking (MobiCom), Chicago, Illinois, USA*, 2010
14. SD Perli, N Ahmed, D Katabi, PixNet: interference-free wireless links using LCD-camera pairs, in *International Conference on Mobile Computing and Networking (MobiCom), Chicago, Illinois, USA*, 2010
15. T Hao, R Zhou, G Xing, COBRA: color barcode streaming for smartphone systems, in *International Conference on Mobile Systems, Applications and Services (MobiSys), Lake District, UK*, 2012
16. S Kuzdeba, AM Wyglinski, B Hombs, *Prototype Implementation of a Visual Communication System Employing Video Imagery, presented at the IEEE Consumer Communications and Networking Conference (CCNC), Las Vegas, NV, USA (11–14 Jan)*, 2013
17. S Arai, S Mase, T Yamazato, T Yendo, T Fujii, M Tanimoto et al., *Feasible Study of Road-to-Vehicle Communication System Using LED Array and High-Speed Camera, presented at the 15th World Congress on ITS, USA*, 2008
18. MRH Mondal, J Armstrong, Analysis of the effect of vignetting on MIMO optical wireless systems using spatial OFDM. J. Lightw. Technol. **32**(5), 922–929 (2014)
19. W Yuan, K Dana, M Varga, A Ashok, M Gruteser, N Mandayam, Computer vision methods for visual MIMO optical system, in *IEEE Computer Society Conference on Computer Vision and Pattern Recognition Workshops (CVPRW), Colorado, USA*, 2011, pp. 37–43
20. MDA Mohamed, S Hranilovic, Two-dimensional binary halftoned optical intensity channels. IET Communications, Special Issue on Optical Wireless Communication Systems **2**(1), 11–17 (2008)
21. A Dabbo, S Hranilovic, Receiver design for wireless optical MIMO channels with magnification, in *10th International Conference on Telecommunications, Zagreb, Croatia*, 2009
22. C Pei, Z Zhang, S Zhang, *SoftOC: Real-Time Projector-Wall-Camera Communication System, presented at the IEEE International Conference on Consumer Electronics (ICCE), Las Vegas, NV, USA*, 2013
23. LL Hanzo, Y Akhtman, L Wang, M Jiang, *MIMO-OFDM for LTE, WiFi and WiMAX: Coherent versus Non-Coherent And Cooperative Turbo Transceivers* (John Wiley & Sons Ltd., Oct. 2010)
24. MRH Mondal, SP Majumder. Analytical performance evaluation of space time coded MIMO OFDM systems impaired by fading and timing jitter, Journal of Communications. **4**(6) (2009)
25. A Loulou, M Renfors, Enhanced OFDM for fragmented spectrum use in 5G systems. Transactions on Emerging Telecommunications Technologies **26**(1), 31–45 (2015)
26. MRH Mondal, KR Panta, J Armstrong, Performance of two dimensional asymmetrically clipped optical OFDM, in *2010 IEEE Globecom Workshops (GC'10), Piscataway, NJ, USA*, 2010
27. MRH Mondal, J Armstrong, Impact of linear misalignment on a spatial OFDM based pixelated system, in *Asia Pacific Conference on Communications (APCC), Jeju Island, South Korea*, 2012
28. MRH Mondal, J Armstrong, The effect of defocus blur on a spatial OFDM optical wireless communication system, in *14th International Conference on Transparent Optical Networks (ICTON), Coventry, England, UK*, 2012
29. MRH Mondal, K Panta, *Performance Analysis of Spatial OFDM for Pixelated Optical Wireless Systems, Transactions on Emerging Telecommunications Technologies (ETT)*, 2015
30. Q Pu, W Hu, *Smooth Transmission over Unsynchronized VLC links, presented at the International Conference on Emerging Networking Experiments and Technologies (CoNEXT) Student Workshop Nice, France*, 2012
31. J Armstrong, AJ Lowery, Power efficient optical OFDM. Electron. Lett. **42**(6), 370–372 (2006)
32. SK Wilson, J Armstrong, *Digital Modulation Techniques for Optical Asymmetrically-Clipped OFDM, presented at the in Proceedings IEEE WCNC, Las Vegas, USA*, 2008
33. K Asadzadeh, A Dabbo, S Hranilovic, Receiver design for asymmetrically clipped optical OFDM, in *GLOBECOM Workshops (GC Wkshps), 2011 IEEE*, 2011, pp. 777–781
34. S Hranilovic, FR Kschischang, Short-range wireless optical communication using pixelated transmitters and imaging receivers, in *IEEE Int. Conf. Commun*, 2004, pp. 891–895
35. MDA Mohamed, A Dabbo, S Hranilovic, MIMO optical wireless channels using halftoning, in *IEEE International Conference on Communications 2008, Beijing, China*, 2008
36. M Tico, M Vehvilainen, Estimation of motion blur point spread function from differently exposed image frames, in *Signal Processing Conference, 2006 14th European*, 2006, pp. 1–4
37. TF Chan, W Chiu-Kwong, Total variation blind deconvolution. IEEE Trans. Image Process. **7**(3), 370–375 (1998)
38. YL You, M Kaveh, A regularization approach to joint blur identification and image restoration. IEEE Trans. Image Process. **5**(3), 416–428 (1996)
39. A Agrawal, X Yi, Coded exposure deblurring: optimized codes for PSF estimation and invertibility, in *Computer Vision And Pattern Recognition, 2009. CVPR 2009. IEEE Conference on*, 2009, pp. 2066–2073
40. C Chung-Hao, C TeYu, Y Wen-Chao, W Che-Yen, Restoration of linear motion and out-of-focus blurred images in surveillance systems, in *Intelligence and Security Informatics, 2008. ISI 2008. IEEE International Conference on*, 2008, pp. 239–241